Efficient prediction of topological superlattice bands with spin-orbit coupling

M. Nabil Y. Lhachemi, ¹ Valentin Crépel, ² and Jennifer Cano^{1,3}

¹Department of Physics and Astronomy, Stony Brook University, Stony Brook, New York 11794, USA

²Department of Physics, University of Toronto, 60 St. George Street, Toronto, ON, M5S 1A7 Canada

³Center for Computational Quantum Physics, Flatiron Institute, New York, New York 10010, USA

(Dated: November 24, 2025)

We develop a symmetry indicator framework to efficiently predict the topology of superlattice-induced minibands with spin-orbit coupling. Our algorithm requires input only from the parent material before the superlattice is applied. The simplification arises by assuming a perturbatively weak superlattice potential; however, our results extend beyond the perturbative regime as long as the superlattice-induced gaps remain open. We first consider a time-reversal- and inversion-symmetric system subject to a weak superlattice potential and derive a compact formula for the \mathbb{Z}_2 invariant of the lowest miniband. We then extend to time-reversal breaking systems and compute the Chern number. We apply our theory to selected transition metal dichalcogenides, $\operatorname{HgTe}/\operatorname{CdTe}$ quantum wells, and thin films of three-dimensional topological insulators and Dirac semimetals. We find topological superlattice bands can arise even from non-topological materials, broadening the pool of candidates for realizing topological flat bands. Our theory predicts which geometry and periodicity of superlattice will yield topological bands for a given material, providing a clear guiding principle for designing topological superlattice heterostructures.

I. INTRODUCTION

Moiré materials provide a highly tunable platform to engineer electronic structures and correlations by producing a large-scale periodicity that folds the Brillouin zone to produce narrow minibands [1–3]. In addition to intrinsic moiré modulations, externally patterned superlattices (SLs) – produced via dielectric patterning or nanopatterned gates – can impose a periodic potential with programmable symmetry and geometry without the need for twisting, thereby enabling miniband engineering on a wider class of two-dimensional (2D) materials [4–8]. Both moiré and nanopatterned SL materials provide the opportunity to tunably create and control topological bands [9–46].

Determining the topological phase diagram of a particular moiré material conventionally requires computing the complete band structure. While this task is accurate, it is often computationally costly and lacks analytical transparency [47–51]. Symmetry indicators offer a complementary route by diagnosing topology from the symmetry eigenvalues (or irreducible representations) at high-symmetry momenta [52–57]. For example, in inversion- and time-reversal-symmetric settings, the Fu-Kane \mathbb{Z}_2 index reduces to a simple product over parity eigenvalues at time-reversal invariant momenta (TRIMs) [52], while in rotation-symmetric settings, indicator formulas constrain the Chern number [53].

A recent theoretical framework introduced symmetry indicators that predict the Chern number of a superlattice miniband using only data from the original monolayer, allowing efficient prediction of the superlattice band topology [58]. However, that result was derived for non-degenerate bands in the absence of spin-orbit coupling (SOC), which excludes many 2D materials and, in particular, does not predict the \mathbb{Z}_2 index.

In this paper, we develop a symmetry-indicator

framework to determine the topology of superlattice bands in the presence of SOC. This covers two important topological indices: the \mathbb{Z}_2 index in the presence of timereversal and inversion symmetry [52], and the Chern number in the absence of time-reversal symmetry, but presence of rotation symmetry [53]. Our results are valid for perturbative values of the SL potential and depend only on the superlattice geometry and a small number of form factors constructed from parent wavefunctions. These formulas remain valid so long as the SL-opened gaps at high-symmetry momenta do not close. While prior studies have explored related concepts in isolated settings [59-62], we present a unified prescription for analytic determination of the \mathbb{Z}_2 invariant and Chern number, allowing rapid application for new moiré systems. We benchmark our approach on spin-valleylocked transition metal dichalcogenides (TMDs) [63] and the Bernevig-Hughes-Zhang (BHZ) model, which describes HgTe/CdTe quantum wells [64], as well as thin films of 3D topological and Dirac materials [65–67]. Our results agree with Refs. [41, 43, 58, 59, 61, 68] where there is overlap.

II. MODEL AND SETUP

A. Hamiltonian

We consider an isolated energy band in a multiband two-dimensional system. In the presence of time-reversal and inversion symmetry, the band will be spin-degenerate. Let $\varepsilon(q)$ and $|\chi(q),s\rangle$ denote the energy and periodic part of the Bloch wavefunction at momentum $k=\gamma+q$ and with z-component of spin $s=\uparrow,\downarrow$, respectively. The momentum γ denotes the conduction band minimum or valence band maximum before application of the superlattice potential. In the

absence of time-reversal-symmetry, we will consider an isolated band with no degeneracy (spin or otherwise), and omit the spin label.

We will apply a superlattice potential whose Fourier decomposition is given by

$$V(r) = -\sum_{g} V_g e^{ig \cdot r}, \qquad (1)$$

where $V_g^* = V_{-g}$ is required for the potential to be real. In this work, we will study the effect of the first harmonics of the superlattice potential. The quasi-momentum k in the original band spans the full Brillouin zone of the original material, which is folded by the superlattice potential into a reduced Brillouin zone (rBZ) defined by the g-vectors. When the system further has inversion-or two-fold rotation-symmetry, $V_{-g} = V_g$ requires the superlattice harmonics to be real.

From these definitions, the Hamiltonian at momentum $k = \gamma + q$ projected into the relevant band is written as

$$H = \sum_{q,g} \sum_{s=\uparrow,\downarrow} \varepsilon(q+g) c_{q+g,s}^{\dagger} c_{q+g,s}$$
$$-\sum_{q,g} \sum_{s,s'} V_g \Lambda_{q+g,q}^{ss'} c_{q+g,s}^{\dagger} c_{q,s'},$$
(2)

where $c_{k,s}^{\dagger}$ creates an electron at momentum k and spin s; q runs over the rBZ; and the form factor is written as $\Lambda_{q,q'}^{ss'} = \langle \chi(q), s | \chi(q'), s' \rangle$.

 $\Lambda_{q,q'}^{ss'} = \langle \chi(q), s | \chi(q'), s' \rangle.$ We are interested in the first miniband populated upon introducing electrons or holes in the superlattice system (electrons if γ denotes the conduction band minimum; holes if γ denotes the valence band maximum); the doping can be accomplished electrostatically via gating. To be concrete, in the following, we will always consider doping the conduction band with electrons and thus derive the topological properties of the lowest energy miniband. Valence band systems can be treated similarly by first applying a particle hole transformation that changes the sign of the Hamiltonian $H \to -H$.

B. Symmetries and gauge-fixing

When we consider systems with time-reversal symmetry (TRS), whose action on spinful fermions is described by an operator \mathcal{T} satisfying $\mathcal{T}^2 = -1$, we fix the gauge of the single-particle states so that \mathcal{T} acts on Kramers partners as

$$\mathcal{T} |\chi(q),\uparrow\rangle = |\chi(-q),\downarrow\rangle,$$

$$\mathcal{T} |\chi(q),\downarrow\rangle = -|\chi(-q),\uparrow\rangle.$$
(3)

We now turn to crystalline symmetries. Inversion requires degeneracy between $|\chi(q),s\rangle$ and $|\chi(-q),s\rangle$; combined with TRS this enforces an exact spin-degeneracy of the band at all q-points. We choose a

gauge in which the action of the inversion operator \mathcal{I} on Kramers partners s for all q in the rBZ is given by

$$\mathcal{I}|\chi(q),s\rangle = \zeta(\gamma)|\chi(-q),s\rangle, \quad \zeta(\gamma) = e^{\pi i \nu(\gamma)}, \quad (4)$$

where we define $\zeta(\gamma)$ as the \mathcal{I} eigenvalue evaluated at γ and $\nu(\gamma) \in \mathbb{Z}_2$.

We now consider a similar gauge-fixing procedure for rotation symmetry. We denote by C_n the largest subgroup of the point symmetry group at γ under which the superlattice potential is invariant. Under a $2\pi/n$ rotation, denoted by R_n , it follows that $\varepsilon(R_nq) = \varepsilon(q)$ and $V_{R_ng} = V_g$. Similar to the \mathcal{I} symmetry case, we choose a gauge in which the action of R_n on a state is given by a representation U_n which satisfies

$$U_n |\chi(q), s\rangle = \lambda_n^{ss'}(\gamma) |\chi(R_n q), s'\rangle.$$
 (5)

In what follows, we only consider rotations about the z-axis, which implies that $\lambda_n^{ss'}(\gamma) = \delta_{ss'}\lambda_n(\gamma)$, with $\lambda_n(\gamma) = \mathrm{e}^{\frac{2\pi i}{n}(\mu_n(\gamma) + \frac{1}{2})}$ being the \mathcal{C}_n eigenvalue evaluated at γ and $\mu_n(\gamma) \in \mathbb{Z}$. The extra factor of 1/2 in the exponent is added to ensure $\mathcal{C}_n^n = -1$, which is valid for spin-1/2 particles.

C. Method and outline

As explained above, we denote as γ the conduction band minimum of a given material, and we determine the topology of the lowest-energy miniband created by the superlattice potential by applying symmetrybased topological indicator formulas. The required symmetry eigenvalues at the high-symmetry points of the superlattice Brillouin zone are obtained using degenerate perturbation theory in the amplitudes of the superlattice In Sec. III we carry out this program harmonics. for inversion- and time-reversal-symmetric systems using the Fu-Kane formula, and in Sec. IV we extend it to TRS-breaking with SOC in rotation symmetric systems. Finally, in Sec. V we apply these formulas to several relevant material platforms.

III. KRAMERS DEGENERATE BANDS

A. Symmetry indicator formula

We begin by examining systems that respect both TRS and inversion-symmetry, which together ensure that all bands are spin-degenerate. While the Chern number of each spin-degenerate band must vanish due to TRS, its topology is captured through the \mathbb{Z}_2 index [69]. In the presence of inversion symmetry, the \mathbb{Z}_2 invariant can be computed using the Fu-Kane formula [52], whereby the \mathbb{Z}_2 index is computed from the product of inversion eigenvalues evaluated at the TRIM.

We label the TRIM by γ_i and let $\zeta(\gamma_i) = e^{i\pi\nu(\gamma_i)}$ denote the corresponding inversion eigenvalue. In 2D,

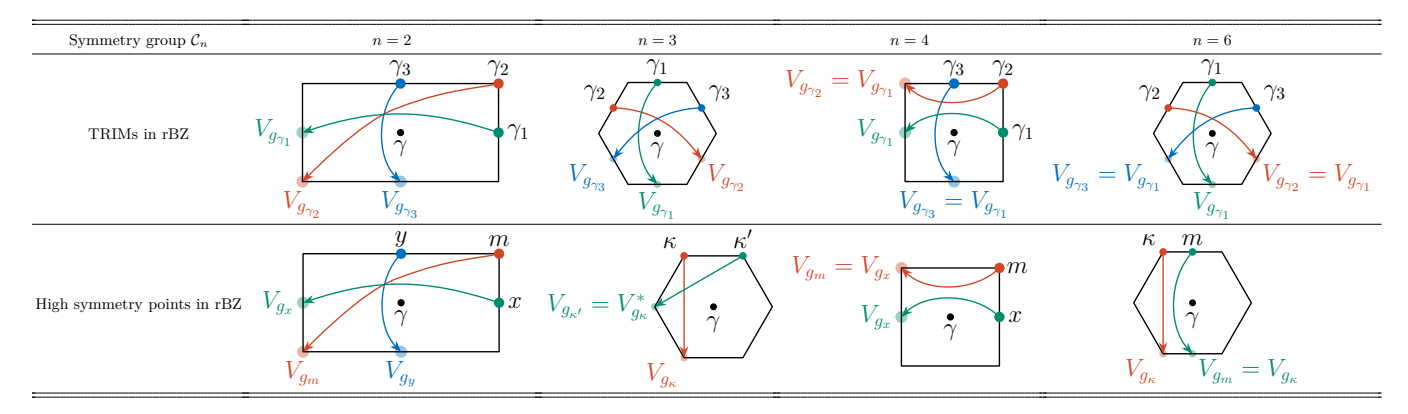


TABLE I: Time-reversal invariant momenta and rotation-invariant points of the rBZ for two-, three-, four- and six-fold rotation-symmetric C_n lattices. These momenta are used in the evaluation of the corresponding symmetry indicator formulas for determining the topology of superlattice mini-bands.

there are four TRIM, shown in Tab. I, including the rBZ center. The Fu-Kane formula is then written as

$$(-1)^{\nu_{\text{FK}}} = \zeta(\gamma)\zeta(\gamma_1)\zeta(\gamma_2)\zeta(\gamma_3), \tag{6}$$

with $\nu_{FK} \in \mathbb{Z}_2$.

In the rest of the section, we determine whether the lowest superlattice-induced miniband from the γ -valley is topological by evaluating the Fu-Kane formula (Eq. 6) through an analytical solution of the band-projected superlattice Hamiltonian (Eq. 2) at the TRIMs, under a perturbative treatment of V(r). The topological invariants derived from this degenerate perturbation analysis remain valid for non-perturbative superlattice amplitudes, provided that the gaps opened at small V(r) persist as the amplitude is increased to its full value.

B. Degenerate perturbation theory

We now seek the inversion eigenvalue of the lowest energy band at the TRIM point $\gamma_i \neq \gamma$ in the rBZ. The γ point is discarded because its \mathcal{I} -eigenvalue $\zeta(\gamma)$ is determined by the original material and is unchanged by the superlattice potential.

The Hamiltonian of Eq. 2 can be diagonalized at γ_i using degenerate perturbation theory by projecting H onto the subspace of degenerate eigenvectors. To determine this subspace, we rely on symmetry: suppose the system is invariant under a rotation $C_{n=2,4,6}$. Then γ_i has point group symmetry C_p , where p=2,4 divides n (p=6 does not occur since $\gamma_i \neq \gamma$) and the degenerate subspace is given by $\{|\chi(q),s\rangle \mid q \in \mathcal{B}(\gamma_i) \text{ and } s=\uparrow,\downarrow\}$ with

$$\mathcal{B}(\gamma_i) = \{ q_k = R_p^k \gamma_i \, | \, k = 0, \dots, p - 1 \}.$$
 (7)

If the system lacks $C_{n=2,4,6}$ symmetry, the momenta $\pm \gamma_i$ are still degenerate due to inversion symmetry and Eq. 7 applies with p=2 and R_p replaced by \mathcal{I} .

The Hamiltonian projected onto this degenerate subspace can be expressed in a block diagonal form

$$PHP = b_{\uparrow} \oplus b_{\downarrow}, \tag{8}$$

with P the projector onto the subspace $\mathcal{B}(\gamma_i)$. This projection is a good approximation as long as for each harmonic V_g of the potential, V_g is much less than the energy difference between $\epsilon(\gamma_i)$ and $\epsilon(\gamma_i+g)$, whenever $\gamma_i+g\notin\mathcal{B}(\gamma_i)$. In particular, our projection is not valid for perfectly flat bands. The presence of \mathcal{T} , \mathcal{I} and \mathcal{C}_p symmetries guarantee that each block is identical, i.e. $b_{\uparrow}=b_{\downarrow}\equiv b$. The \mathcal{C}_p symmetry further constrains b to be circulant

$$b = \operatorname{circ}(a_0, a_1, \dots, a_{p-1})$$

$$= \begin{pmatrix} a_0 & a_{p-1} & \dots & a_2 & a_1 \\ a_1 & a_0 & \dots & a_3 & a_2 \\ \vdots & \vdots & \ddots & \vdots & \vdots \\ a_{p-2} & a_{p-3} & \dots & a_0 & a_{p-1} \\ a_{p-1} & a_{p-2} & \dots & a_1 & a_0 \end{pmatrix}.$$

$$(9)$$

with $a_0 = \varepsilon_{\gamma_i}$ and

$$a_{k>0} = -\Lambda_{q_k,\gamma_i}^{\uparrow} V_{q_k-\gamma_i} = a_{p-k}^*. \tag{10}$$

Here, we define $\Lambda_{q_k,\gamma_i}^{\uparrow} = \langle \chi(q_k), \uparrow | \chi(\gamma_i), \uparrow \rangle$. The eigenvalues and eigenvectors of b are obtained by discrete Fourier transform; see App. A for details. The result is that the eigenvalues of Eq. 8 are doubly degenerate and given by

$$E_{\nu} = \sum_{k=0}^{p-1} \omega_p^{\nu k} a_k, \tag{11}$$

with eigenvectors

$$|\varphi_{\nu,s}\rangle = \sum_{k=0}^{p-1} \frac{\omega_p^{-\nu k}}{\sqrt{p}} |\chi(q_k), s\rangle, \qquad (12)$$

where $\omega_p = e^{2\pi i/p}$ represents the *p*-th root of unity and $\nu = 0, 1, \dots, p-1$. Using Eq. 4, the \mathcal{I} -eigenvalues of these eigenvectors are then

$$\langle \varphi_{\nu,s} | \mathcal{I} | \varphi_{\nu,s} \rangle = \omega_2^{\nu} \zeta(\gamma).$$
 (13)

The \mathcal{I} -eigenvalues obtained above are associated to the p lowest-energy minibands at γ_i in the rBZ. To obtain the inversion eigenvalue of the *lowest* energy miniband, we need to find to which value of ν it corresponds, i.e., find the smallest E_{ν} . For the two relevant cases, p=2,4, Eq. 11 is rewritten as

$$E_{\nu} = a_0 + \begin{cases} \operatorname{Re}(\omega_2^{\nu} a_1), & p = 2\\ \operatorname{Re}(2\omega_4^{\nu} a_1 + \omega_2^{\nu} a_2), & p = 4 \end{cases} . \tag{14}$$

Assuming that for p=4 the leading harmonics of the potential dominate over the second one, we set $a_2=0$. The lowest miniband is then obtained by minimizing E_{ν} with respect to ν , which yields $\nu=-p\arg\left(\Lambda_{q_1,\gamma_i}^{\uparrow}V_{g_{\gamma_i}}\right)/2\pi \mod p$, where we have defined $g_{\gamma_i}=q_1-\gamma_i$. However, since E_{ν} is only defined for integer ν , we seek the nearest integer to this value,

$$\nu_p(\gamma_i) = \left| \frac{\pi - \Phi_{\gamma_i}^{\uparrow,\circlearrowleft}}{2\pi} \right|, \quad \Phi_{\gamma_i}^{\uparrow,\circlearrowleft} = p \arg\left(\Lambda_{q_1,\gamma_i}^{\uparrow} V_{g_{\gamma_i}}\right), \quad (15)$$

where $\lfloor x \rfloor$ represents the largest integer smaller than x. The phase $\Phi_{\gamma_i}^{\uparrow,\circlearrowleft}$ represents the accumulated phase arising from the Berry phase and the harmonics of the potential as the wave function is transported along the discrete loop $L_p^{\uparrow} = \{q_k = R_p^k \gamma_i\}_{k=0,\dots,p-1}$, which links TRIMs in the same spin sector.

Combining Eq. 13 and Eq. 15 gives the \mathcal{I} -eigenvalues

$$\nu(\gamma_i) = \nu(\gamma) + \nu_n(\gamma_i). \tag{16}$$

This result shows how the \mathcal{I} -eigenvalues are affected by the superlattice potential through the dependence of $\nu_p(\gamma_i)$ on the potential harmonics and the form factors of the material. Hence, Eq. 16 can be used in Eq. 6 to compute the Fu-Kane invariant of the lowest superlattice-induced miniband, as we now describe.

C. Topological invariants

We now calculate the Fu-Kane invariant by plugging the inversion eigenvalues in Eq. 16 into Eq. 6. This yields

$$\nu_{\text{FK}} = \sum_{\gamma_i \neq \gamma} \nu_p(\gamma_i) \mod 2, \tag{17}$$

where γ_i runs over the non-trivial TRIMs of the rBZ, $\nu_p(\gamma_i)$ is given in Eq. 15 and $p=p(\gamma_i)$ is the largest divisor of n such that $R_n^{n/p}\gamma_i=\gamma_i$ (or $p(\gamma_i)=2$ in the absence of $\mathcal{C}_{n=2,4,6}$ symmetry). Note that the contribution from the γ point in Eq. 17 appears four times, once for each TRIM, and consequently disappears since $\nu_{\rm FK}$ is defined modulo 2, i.e. $4\nu(\gamma)=0 \mod 2$.

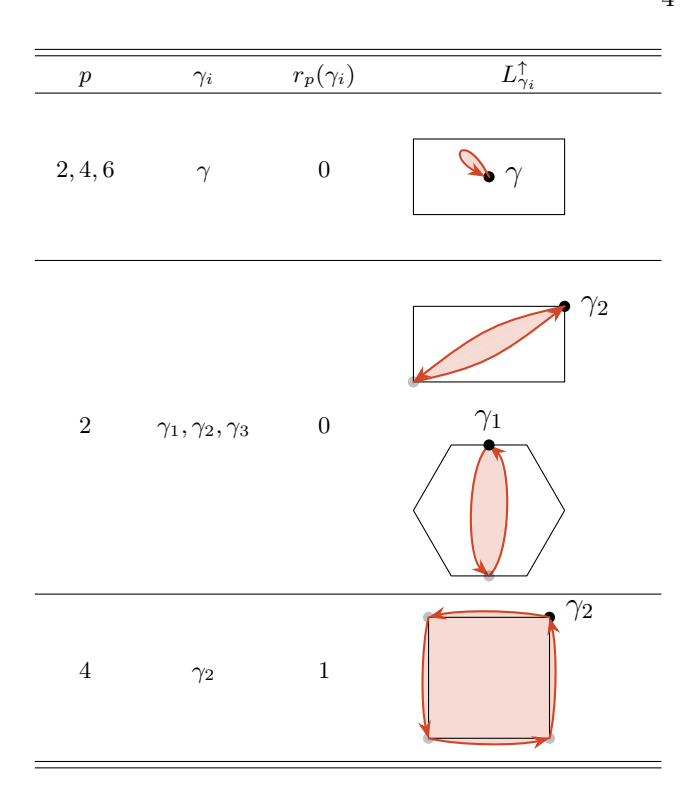


TABLE II: Geometric factor $r_p(\gamma_i)$, defined as the fraction of the rBZ spanned by $L_{\gamma_i}^{\uparrow}$ for all TRIMs. The last column shows the enclosed area in red with the rBZ outlined in black; in the first two cases, the red area vanishes as the loop contracts to a point or a line.

Eq. 17 can be simplified when there is a rotation symmetry with n > 3. Specifically, for n = 2 or n = 3, none of the TRIM are symmetry-equivalent, so the Fu-Kane invariant cannot be simplified beyond Eq. 17,

$$\nu_{\text{FK}}^{(2),(3)} = \sum_{\gamma_i \neq \gamma} \nu_2(\gamma_i) \mod 2.$$
 (18)

The difference between the n=2 and the n=3 cases is the location of the TRIM in the rBZ; see Tab. I. For n=4, the TRIM at x and y are symmetry-equivalent and hence $\nu_2(x)=\nu_2(y)$. Since $\nu_{\rm FK}$ is defined modulo 2, these terms cancel each other, which implies

$$\nu_{\text{FK}}^{(4)} = \nu_4(m) \mod 2.$$
 (19)

Similarly, for n=6, there are three TRIM located at m and its counterparts related by six-fold rotation, for which $\nu_2(m) = \nu_2(R_6 m) = \nu_2(R_6^{-1} m)$. Thus

$$\nu_{\text{FK}}^{(6)} = \nu_2(m) \mod 2.$$
 (20)

D. Long wavelength limit

In the long wavelength limit, where the primitive reciprocal lattice vectors of the rBZ are small compared to the typical scale on which the quantum geometry of the original band varies, the phase factor $\Phi_{\gamma_i}^{\uparrow,\circlearrowleft}$ can be simplified. Using the \mathcal{C}_p symmetry, it is rewritten as

$$\Phi_{\gamma_i}^{\uparrow,\circlearrowleft} = p \arg\left(V_{g_{\gamma_i}}\right) + \arg\left(\prod_{k=0}^{p-1} \Lambda_{q_{k+1},q_k}^{\uparrow}\right)
\simeq p \arg\left(V_{g_{\gamma_i}}\right) + r_p(\gamma_i)\phi_B^{\uparrow},$$
(21)

where $\phi_B^{\uparrow} = \Omega_{\gamma}^{\uparrow} A_{\rm rBZ}$ is the total Berry flux enclosed by the rBZ, $\Omega_{\gamma}^{\uparrow}$ is the Berry curvature at γ of the spin-up band and $r_p(\gamma_i)$ denotes the fraction of the rBZ area $A_{\rm rBZ}$ enclosed by the loop L_p^{\uparrow} . For the two cases considered in this calculation, $r_2(\gamma_i) = 0$ and $r_4(\gamma_i) = 1$ (see Tab. II). More precisely, we find

$$\nu_{\text{FK}}^{(2),(3)} = \frac{1}{\pi} \arg(V_{g_{\gamma_1}} V_{g_{\gamma_2}} V_{g_{\gamma_3}}), \tag{22a}$$

$$\nu_{\rm FK}^{(4)} = \left| \frac{\pi - \phi_B^{\uparrow}}{2\pi} \right|, \tag{22b}$$

$$\nu_{\text{FK}}^{(6)} = \frac{1}{\pi} \arg(V_{g_{\gamma_2}}),$$
(22c)

where the definitions of the superlattice harmonics are shown in Tab. I. This indicates a striking difference between systems that have C_4 symmetry and those that do not: in the long wavelength limit, for n=2,3,6, the topology is governed exclusively by the sign of the superlattice harmonics; in contrast, for n=4, the sign of the harmonics cancels out and only the Berry curvature contribution can produce a non-trivial topology.

IV. TIME REVERSAL BREAKING SYSTEMS WITH SOC

In this section, we apply our methodology to systems with SOC that break time-reversal symmetry, which in turn lifts the spin degeneracy. We show how the approach presented above can be used to obtain the Chern number C_n of the lowest-energy miniband induced by an external superlattice potential. The results obtained in this section are similar to the non-interacting results presented in Ref. [58], which considered the same problem in the absence of SOC.

A. Symmetry indicator formula

We consider a non-degenerate band in a system with broken time-reversal symmetry. We assume that γ remains invariant under an n-fold rotation; γ need not be a TRIM. With these conditions, the projected Hamiltonian takes the same form as Eq. 2, but with the spin sum omitted,

$$H = \sum_{q,g} \varepsilon(q+g) c_{q+g}^{\dagger} c_{q+g} - \sum_{q,g} V_g \Lambda_{q+g,q} c_{q+g}^{\dagger} c_q, \quad (23)$$

where $\Lambda_{q,q'} = \langle \chi(q) | \chi(q') \rangle$. To include rotation symmetry, we adopt the gauge given in Eq. 5. To characterize the topology, we apply the symmetry indicator formula for the Chern number C given in Ref. [53]. Specifically, for an isolated band with R_n symmetry, C is determined modulo n by the product of $\lambda_p(q_p)$, the R_p eigenvalues of its Bloch eigenvectors at the R_p -invariant momenta q_p in the rBZ, where p is any divisor of n. Explicitly,

$$\begin{cases} e^{\frac{2\pi i}{2}C_{2}} = \lambda_{2}(\gamma)\lambda_{2}(m)\lambda_{2}(x)\lambda_{2}(y) & \text{for } n = 2\\ e^{\frac{2\pi i}{3}C_{3}} = (-1)^{F}\lambda_{3}(\gamma)\lambda_{3}(\kappa)\lambda_{3}(\kappa') & \text{for } n = 3\\ e^{\frac{2\pi i}{4}C_{4}} = (-1)^{F}\lambda_{4}(\gamma)\lambda_{4}(m)\lambda_{2}(x) & \text{for } n = 4 \end{cases}, (24)$$

where $C_n = C \mod n$ and F is twice the total spin of the particle. In our case, we are considering spin-1/2 electrons, so F = 1.

B. Degenerate perturbation theory

Degenerate perturbation theory can now be employed to determine the eigenvalues λ_p . Let q_0 denote a high-symmetry point in the rBZ with point group symmetry \mathcal{C}_p , distinct from the γ point. Excluding the γ point restricts p=2,3,4. For sufficiently weak superlattice potentials, Eq. 23 may be diagonalized using degenerate perturbation theory. The Hamiltonian H is projected onto the subspace spanned by $\{|\chi(q)\rangle|q\in\mathcal{B}(q_0)\}$, where $\mathcal{B}(q_0)$ is defined in Eq. 7. The symmetry \mathcal{C}_p further constrains the projected Hamiltonian to take a circular form, such that PHP=b, with b having the same structure as Eq. 9, but with matrix elements specified by $a_0=\varepsilon_{q_0}$ and

$$a_{k>0} = -\Lambda_{q_k,q_0} V_{q_k-q_0} = a_{p-k}^*.$$
 (25)

The eigenvalues of the projected Hamiltonian are therefore the same as Eq. 11 and the eigenvectors are given by Eq. 12 without the spin index. The R_p -eigenvalue of the eigenstate ϕ_{μ} is given by:

$$\langle \phi_{\mu} | U_p | \phi_{\mu} \rangle = \lambda_n^{n/p} (\gamma) \omega_p^{\mu}.$$
 (26)

The remaining step is to identify which value of μ corresponds to the lowest energy miniband of the rBZ, i.e., for which value of μ the energy E_{μ} is minimized. For the relevant values of p,

$$E_{\mu} = a_0 + \begin{cases} \operatorname{Re}(\omega_2^{\mu} a_1), & p = 2\\ \operatorname{Re}(2\omega_3^{\mu} a_1), & p = 3\\ \operatorname{Re}(2\omega_4^{\mu} a_1 + \omega_2^{\mu} a_2), & p = 4 \end{cases}$$
(27)

which after minimization with respect to μ gives

$$\mu_p(q_0) = \left| \frac{\pi - \Phi_{q_0}^{\circlearrowleft}}{2\pi} \right|, \tag{28}$$

where we defined the phase $\Phi_{q_0}^{\circlearrowleft} = p(q_0) \arg(\Lambda_{q_1,q_0} V_{g_{q_0}})$. This phase represents the combined phase coming from the Berry phase and the potential harmonic as the wave function is transported along the discrete loop $L_p = \{q_k = R_p^k q_0\}_{k=0,\dots,p-1}$ linking degenerate high-symmetry points. In the limit of a large superlattice, we simplify further by approximating the Berry phase as a constant over the rBZ. Then the discrete Berry phase is given by $r_p(q_0)\phi_B$, where $\phi_B = \Omega_\gamma A_{\rm rBZ}$ is the Berry phase enclosed by the entire BZ, with Ω_γ the Berry curvature at γ , and $r_p(q_0)A_{\rm rBZ}$ is the area enclosed by the loop L_p . Together, in this limit $\Phi_{q_0}^{\circlearrowleft} \simeq p(q_0) \arg(V_{g_{q_0}}) + r_p(q_0)\phi_B$ [58].

Together, Eq. 26 and Eq. 28 give the following formula for the R_p -eigenvalues of the lowest energy superlattice band at each high-symmetry point q_0

$$\lambda_p(q_0) = e^{\frac{2\pi i}{p} \left[\mu_n(\gamma) + \mu_p(q_0) + \frac{1}{2} \right]}.$$
 (29)

This result demonstrates that the R_p -eigenvalues are modified by the external superlattice potential through the dependence of $\mu_p(q_0)$ on both the potential harmonics and the form factors. These eigenvalues may then be incorporated into the symmetry-indicator expressions of Eq. 24, to evaluate the Chern number of the lowest miniband in the rBZ, as we now describe.

C. Topological invariants

Inserting Eq. 29 in Eq. 24 gives for the Chern number

$$C_n = \left(\mu_n(\gamma) + \frac{1}{2}\right) \sum_{q_0} \frac{n}{p(q_0)} + \sum_{q_0 \neq \gamma} \frac{n}{p(q_0)} \mu_p(q_0)$$

$$+ \frac{nF}{2} (1 - \delta_{n2}) \mod n$$

$$= \sum_{q_0 \neq \gamma} \frac{n}{p(q_0)} \mu_p(q_0) \mod n,$$
(30)

where q_0 runs over all high-symmetry points of the rBZ listed in Eq. 24, including γ , unless otherwise stated, and $p(q_0)$ is the largest divisor of n such that $R_n^{n/p}q_0=q_0$. Observe that since $p(q_0)$ divides n, the ratio $n/p(q_0)$ is an integer. To obtain the last equality, we used F=1, $\mu_n(\gamma)\in\mathbb{Z}$ and the fact that C_n is defined modulo n. Notice that the spin-contribution – the 1/2 factor of Eq. 29 – cancels out the $(-1)^F$ in Eq. 24. This cancellation implies that the resulting expression for the Chern number with respect to the R_p -eigenvalues coincides with the result reported in Ref. [58], where no SOC was considered. Hence, for values of the superlattice potential that preserve the gaps at the high-symmetry points, the symmetry indicator formalism yields identical results with or without SOC.

V. APPLICATIONS

In this section, we apply the main results of Secs. III and IV to concrete models. We begin with the Bernevig-Hughes-Zhang (BHZ) model, which describes materials such as HgTe quantum wells. This general model preserves both \mathcal{T} and \mathcal{I} symmetry and is therefore suited to the \mathbb{Z}_2 criterion of Eq. 17 when an inversion- and C_n -symmetric superlattice potential (SL_n) is considered. Next, we consider thin films of 3D topological insulators and Dirac semimetals that retain \mathcal{T} and \mathcal{I} symmetry and can be described by the continuum version of the BHZ model, implying that the same invariant can classify the topology of these quasi-2D systems. Finally, we examine the continuum model of monolayer transition metal dichalcogenides (TMDs), whose non-degenerate spin-valley locked bands break \mathcal{T} symmetry in each valley, allowing the use of Eq. 30 to predict the topology of the SL_n -induced minibands in each valley.

One common feature of all these materials is that they can be modeled by variants of the following Hamiltonian

$$h_{\xi_x \xi_y}(\mathbf{k}) = d_0 + \xi_x d_x \sigma_x + \xi_y d_y \sigma_y + d_z \sigma_z, \tag{31}$$

where $\xi_{i=x,y}=\pm 1$ and the form of the real coefficients $d_0,\ d_x,\ d_y$ and d_z depend on ${\bf k}$ and the material under consideration. The eigenenergies of this two band Hamiltonian are $E_\pm=d_0\pm d$ with $d=\sqrt{d_x^2+d_y^2+d_z^2}$ and the corresponding eigenvectors can be written as

$$\left| \Psi_{+}^{\xi_{x},\xi_{y}} \right\rangle = \frac{1}{\mathcal{N}} \begin{pmatrix} d_{z} + \operatorname{sign}(d_{z})d \\ \xi_{x}d_{x} + i\xi_{y}d_{y} \end{pmatrix},
\left| \Psi_{-}^{\xi_{x},\xi_{y}} \right\rangle = \frac{1}{\mathcal{N}} \begin{pmatrix} -\xi_{x}d_{x} + i\xi_{y}d_{y} \\ d_{z} + \operatorname{sign}(d_{z})d \end{pmatrix},$$
(32)

with $\mathcal{N}=\sqrt{2d(d+|d_z|)}$, and where the kinks in the coefficients of the eigenvectors as d_z crosses zero correspond to switching to a different gauge – a requirement for topological system that cannot accommodate a smooth gauge throughout the rBZ [43]. Below we use these general eigenfunctions to calculate the form factors of each material under consideration and apply the topological invariant formula derived in the previous sections.

A. SL_n -BHZ

1. Phase diagram without superlattice

The BHZ model is a minimal model that can describe the quantum spin Hall effect observed in certain two dimensional topological insulators [64]. In the basis $\{|E,\uparrow\rangle,|H,\uparrow\rangle,|E,\downarrow\rangle,|H,\downarrow\rangle\}$, where E and H represent orbitals with opposite parity and the arrows represent the z-component of spin, the lattice BHZ model can be written as a block diagonal Hamiltonian, where each

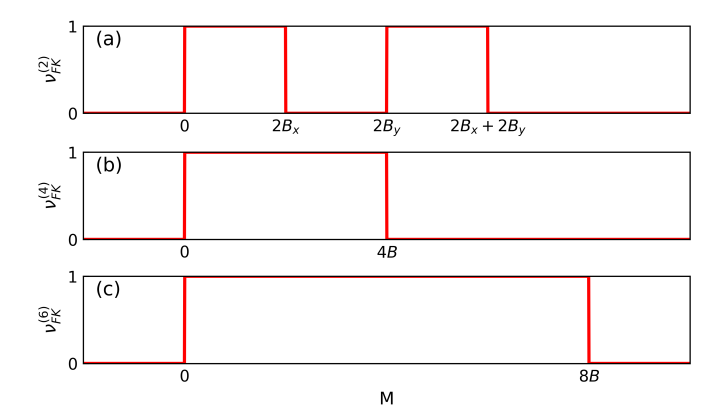


FIG. 1: Phase diagrams of the (a) rectangular, (b) square and (c) triangular lattice BHZ model without a superlattice potential. (The parameters C, D_j and A do not affect the topological phase diagram.)

block represents a spin sector

$$h_{\rm BHZ}(\mathbf{k}) = h_{+}(\mathbf{k}) \oplus h_{-}(\mathbf{k}), \tag{33}$$

with $h_{\xi}(\mathbf{k})$ having the same form as the Hamiltonian in Eq. 31 with $\xi_x = \xi$, $\xi_y = 1$ and

$$d_{0}(\mathbf{k}) = C - \sum_{j} D_{j} (1 - \cos \mathbf{k} \cdot \boldsymbol{\delta}_{j})$$

$$d_{z}(\mathbf{k}) = M - \sum_{j} B_{j} (1 - \cos \mathbf{k} \cdot \boldsymbol{\delta}_{j})$$

$$d_{x}(\mathbf{k}) = A \sum_{j} \hat{\delta}_{j} \cdot \hat{x} \sin \mathbf{k} \cdot \boldsymbol{\delta}_{j}$$

$$d_{y}(\mathbf{k}) = A \sum_{j} \hat{\delta}_{j} \cdot \hat{y} \sin \mathbf{k} \cdot \boldsymbol{\delta}_{j}$$
(34)

Here, $\xi = \pm 1$ labels the spin-up or spin-down block, which are related by $h_{-}(\mathbf{k}) = h_{+}^{*}(-\mathbf{k})$; the sum over j is taken over equivalent bond vectors $\boldsymbol{\delta}$; and C, D_{j} , A, M, B_{j} are material parameters. Note that on a square or triangular lattice, then $D_{j} = D$ and $B_{j} = B$.

The BHZ Hamiltonian is invariant under time-reversal $\mathcal{T} = is_y \mathcal{K}$, which enforces $\mathcal{T}h_{\mathrm{BHZ}}(\mathbf{k})\mathcal{T}^{-1} = h_{\mathrm{BHZ}}(-\mathbf{k})$, and inversion $\mathcal{I} = s_0 \otimes \sigma_z$, which likewise yields $\mathcal{I}h_{\mathrm{BHZ}}(\mathbf{k})\mathcal{I}^{-1} = h_{\mathrm{BHZ}}(-\mathbf{k})$; here s_y acts on spin and \mathcal{K} denotes complex conjugation. With these symmetries, the \mathbb{Z}_2 invariant characterizes the topology of the system. The phase diagram is controlled by the sign of M and the sign of $d_z(\gamma_i)$ where γ_i represents a TRIM. The topological phase diagrams of the BHZ model on different lattices without the SL potential are shown in Fig. 1. In the rest of this section, we will apply the result of Sec. III to study the effect of a SL potential on the BHZ model.

2. Adding the superlattice

Since \mathcal{T} and \mathcal{I} enforce that the form factors are identical for opposite spins, we restrict our attention to

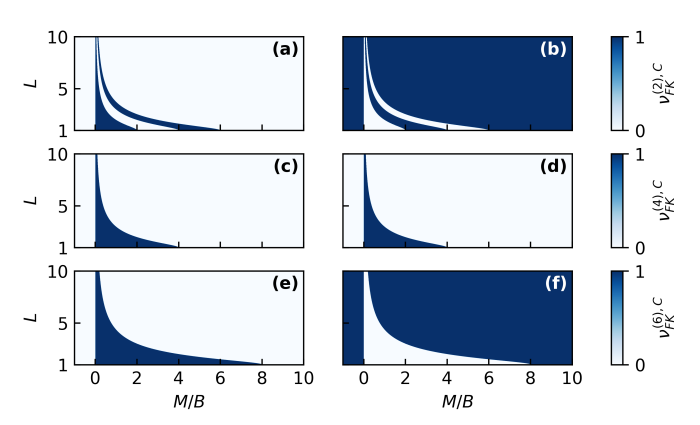


FIG. 2: Phase diagram showing the \mathbb{Z}_2 index of the conduction band for (a-b) $\mathrm{SL}_2\text{-BHZ}_2$, (c-d) $\mathrm{SL}_4\text{-BHZ}_4$ and (e-f) $\mathrm{SL}_6\text{-BHZ}_6$, as a function of M/B and the ratio of the SL periodicity to the original lattice constant $L=a_{\mathrm{SL}}/a$. Here, BHZ_n represents the \mathcal{C}_n symetric BHZ model. In panels (a-b), $B_x=B$ and $B_y=2B$. We fix $A=-3\mathrm{eV}$ in panels (c-d) (A does not enter the \mathbb{Z}_2 invariant for $\mathrm{SL}_{2,6}$.) The left (right) panels show the topological phase diagrams for positive (negative) values of the SL potential harmonics.

the spin-up sector and apply the theory developed in Sec. III to the conduction band. Using Eq. 32, we find the form factors

$$\Lambda_{-q,q}^{\uparrow} = \frac{\langle \Phi_{+}(q) | \mathcal{I} | \Phi_{+}(q) \rangle}{\zeta^{\uparrow}(\gamma)} = \frac{d_{z}(q)}{d(q)} \operatorname{sgn}(M), \quad (35)$$

where $\zeta^{\uparrow}(\gamma) = \langle \Phi_{+}(\gamma) | \mathcal{I} | \Phi_{+}(\gamma) \rangle = \operatorname{sgn}(M)$ represents the parity eigenvalue of the conduction band at γ and we define $|\Phi_{+}\rangle \equiv |\Psi_{+}^{1,1}\rangle$ to simplify the notation.

In the case of a superlattice with two-fold or six-fold symmetry, this form factor, evaluated at the different TRIM in the rBZ, entirely determines the \mathbb{Z}_2 index of the lowest miniband. Specifically, Eq. 15 yields $\nu_2(q) = \arg\left(d_z(q)V_{g_q}M\right)/\pi \mod 2$ at each rBZ-TRIM q. Eqs. 18 and 20 then give the Fu-Kane invariant for the conduction band of SL₂-BHZ and SL₆-BHZ. Namely, for the former

$$\nu_{\text{FK}}^{(2)} = \frac{\arg(M)}{\pi} + \frac{1}{\pi} \sum_{q=x,y,m} \arg(d_z(q)V_{g_q}) \mod 2,$$
(36)

and for the latter

$$\nu_{\text{FK}}^{(6)} = \frac{\arg(M)}{\pi} + \frac{1}{\pi} \arg(d_z(m)V_{g_m}) \mod 2.$$
 (37)

As explained in Sec. II A, the same calculation can be repeated in the valence band by performing a particle-hole transformation. In these formulas, this amounts to flipping $V_g \to -V_g$, $M \to -M$ and $d_z \to -d_z$. The two latter changes cancel out because the only dependence is on products of the form $d_z V_g$, leading to $\nu_{\rm FK}^{(n),{\rm C}} + \nu_{\rm FK}^{(n),{\rm V}} = 1 \mod 2$ for n=2 and 6. Consequently, exactly one

of the two bands carries a non-trivial \mathbb{Z}_2 index: if the conduction (valence) band is topologically non-trivial, then the valence (conduction) band is trivial. The fact that the valence/conduction bands have opposite \mathbb{Z}_2 index was also found in Ref. [43] for SL₆-BHZ.

For SL₄-BHZ, Eq. 19 shows that the relevant form factor is between a momentum q and its four-fold rotated partner R_4q . The p-fold rotation operator for the BHZ Hamiltonian is expressed as

$$U_p = e^{-i\xi \frac{2\pi}{p}J_z},\tag{38}$$

with J_z the z component of the total angular momentum. The basis chosen corresponds to the E orbital carrying $j_E = 1/2$ and the H orbital $j_H = 3/2$ [64]. Thus, the form factor is given by

$$\Lambda_{R_4q,q}^{\uparrow,C} = \frac{\langle \Phi_+(q) | U_4^{\dagger} | \Phi_+(q) \rangle}{\langle \Phi_+(\gamma) | U_4^{\dagger} | \Phi_+(\gamma) \rangle} = \frac{i + \frac{d_z(q)}{d(q)}}{i + \operatorname{sgn}(M)}, \quad (39)$$

and the Fu-Kane invariant is

$$\nu_{\text{FK}}^{(4),C} = \left| \frac{\pi - 4 \arg\left(\Lambda_{R_4 m, m}^{\uparrow, C} V_{g_m}\right)}{2\pi} \right| \mod 2. \quad (40)$$

Fig. 2 displays the calculated topological phase diagrams. The analysis reveals that both the harmonics and the periodicity of the superlattice potential influence the topological character of the $\rm SL_2\text{-}BHZ$, $\rm SL_4\text{-}BHZ$ and $\rm SL_6\text{-}BHZ$ models.

3. Discussion

Comparing the phase diagrams with (Fig. 2) and without (Fig. 1) the superlattice reveals that in the case of SL₂ or SL₆, topological superlattice bands can emerge when the original bands are trivial, and vice versa. In other words, one need not restrict the search for a topological superlattice band to a superlattice imposed on a topological material: a superlattice imposed on a topologically trivial material will suffice as long as there is sufficient spin-orbit coupling that mixes the conduction/valence bands (i.e., A in Eq. 34 must be non-zero so that the putative topological mini-band is gapped). The sign of the superlattice harmonics will determine whether the valence or conduction band of the superlattice band structure is nontrivial. This result has important consequences for material applications, which we will detail momentarily. In summary: the topology of a HgTe/CdTe quantum well, or an ultra-thin film of a 3D topological insulator or Dirac semimetal, depends on its thickness [64, 70-72], but our results show that topological superlattice bands can be obtained independent of that thickness.

The case of the four-fold symmetric superlattice, SL_4 , is different: comparing Fig. 1(b) to Figs. 2(c,d) shows that for SL_4 , a topological superlattice band is

only realized when the original band is also topological. Furthermore, the band topology depends strongly on the ratio $L = a_{\rm SL}/a$, with $a_{\rm SL}$ being the periodicity of the superlattice and a the original fixed lattice constant: when L is too large, the superlattice bands will always This is best understood using our longwavelength approximation (Eq. 22). When n = 4, only the Berry flux enclosed in the rBZ can drive a non-trivial Fu-Kane index, but the latter decreases as $1/a_{\rm SL}^2$ with increasing superlattice period $a_{\rm SL}.$ As a result, it always becomes smaller than π for large enough values of $a_{\rm SL}$, leading to a trivial Fu-Kane index. The exact position of the transition depends on the amount of Berry curvature at γ , which is largest on the topological side of the transition at $M=0^+$. This also explains the asymmetric shape of the topological region: the transition point scales as $a_{\rm SL}^c \sim \sqrt{\Omega_{\gamma}}$, which diverges at the topological transition where the gap closes at γ and then slowly decays as Ω_{γ} decreases and eventually vanishes in the trivial phase at large M.

We now turn to a concrete example in 2D: HgTe/CdTe quantum well heterostructures. These systems can be described by the square lattice BHZ model of Eq. 33. with parameter values that depend on the thickness η of the quantum well. For $\eta = 58\text{Å}$, the parameters are B = -18.0 eV and M = 9.22 meV, and for $\eta = 70 \text{Å}$, B = -16.9 eV and M = -6.86 meV [64]. Without a SL potential, only the second thickness admits a topological phase since M/B > 0 (see Fig. 1) [64]. As discussed in the previous paragraph: for a rectangular or hexagonal superlattice, topological mini bands can be realized for either value of η . For a square superlattice, Fig. 2(c,d) shows that a topological miniband can only be obtained in the topological regime, e.g., with thickness $\eta = 70$ A, and requires a periodicity less than the critical value $L_c =$ 155.9.

B. SL_n -thin films

We apply now our formalism to thin films of 3D Dirac semimetals and topological insulators in the quasi-2D limit, where their bulk and surfaces are gapped. The topology of such films is classified by a \mathbb{Z}_2 index that depends on thickness [70–72].

One example of such a 3D system is Cd_3As_2 , which is a bulk Dirac semimetal [71]. It was shown experimentally that (001) grown Cd_3As_2 thin films (tf Cd_3As_2) can realize a 2D topological insulating phase [73]. The Hamiltonian that describes this material has the same form as Eq. 33 with blocks given by a Dirac Hamiltonian of the form of Eq. 31 with $\xi_x = \xi$, $\xi_y = 1$, $d_0 = E_0 - ck^2$, $d_x = vk_x$, $d_y = -vk_y$ and $d_z = \delta - bk^2$ [61]. The material values are listed in Tab. III. The form factors needed to characterize the topology of SL_n -tf Cd_3As_2 are the same as those presented in Eqs. 35 and 39. Therefore, the Fu-Kane invariant of SL_2 -tf Cd_3As_2 , SL_4 -tf Cd_3As_2 and SL_6 -tf Cd_3As_2 have the same form as Eqs. 36, 40 and

	N	E_0 [eV]	$c \text{ [eV Å}^2]$	v [eV Å]	$b~[{\rm eV~ \mathring{A}^2}]$	$\delta \ [{\rm meV}]$	$SL_{n=2,6} > 0$	$SL_{n=2,6} < 0$	SL_4
Cd_3As_2 [61, 65]	-	0	-11.5	0.889	13.5	Fig. 3	Fig. 3(a, e)	Fig. 3(b, f)	Fig. 3 (c, d)
	2	0.121	-16.14	-0.048	-17.56	119.5	0	1	0
$\mathrm{Bi}_2\mathrm{Se}_3$ [72]	3	0.043	-13.94	1.697	-15.82	41.00	0	1	0
	4	0.018	-13.91	1.920	-16.35	17.00	0	1	0
	5	0.008	-13.23	2.010	-16.51	7.000	0	1	0
	6	-0.002	-13.06	2.046	-16.75	3.000	0	1	0
	2	0.077	-28.41	2.463	-29.14	-76.50	1	0	1
$\mathrm{Bi}_{2}\mathrm{Te}_{3}$ [72]	3	0.013	-27.52	0.876	-28.10	13.50	0	1	0
	4	0.001	-29.55	1.301	-30.06	1.500	0	1	0
	5	0.002	-28.50	1.340	-28.97	-3.000	1	0	1
	2	0.127	-21.70	0.482	-26.29	127.0	0	1	0
Sb_2Te_3 [72]	3	0.030	-15.45	2.921	-16.04	32.00	0	1	0
	4	0.002	-13.39	2.952	-13.89	-3.500	1	0	1
	5	0.008	-12.65	2.870	-13.10	-9.000	1	0	1
	6	0.006	-13.38	2.887	-13.83	-6.000	1	0	1

TABLE III: Numerical values of the parameters in the models considered in Sec. VB applied to thin films of Cd_3As_2 , Bi_2Se_3 , Bi_2Te_3 and Sb_2Te_3 . The last three columns provide the \mathbb{Z}_2 invariant when each system is subject to a SL_n potential. For n=2,6, we consider a superlattice in the long wavelength limit, whereas for n=4 we consider a superlattice with a periodicity smaller than the critical value a_{SL}^c (for a larger periodicity, it is always trivial). In these columns, an entry 0 indicates a topologically trivial phase, while 1 means that the system hosts a quantum spin Hall phase according to our perturbative symmetry indicator framework. The notation $SL_n > 0$ ($SL_n < 0$) indicates that the harmonics of the SL potential are positive (negative).

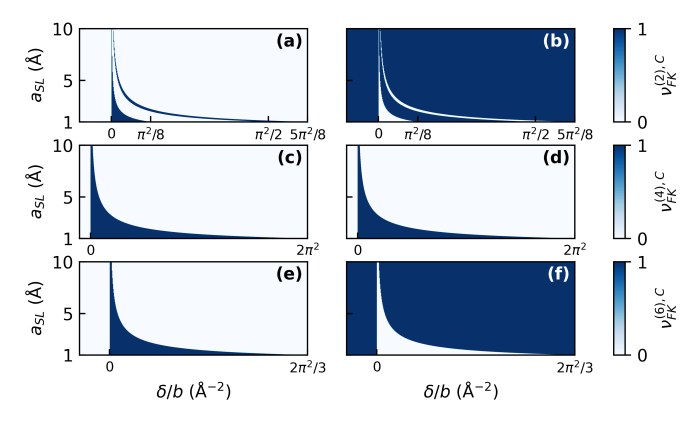


FIG. 3: Topological phase diagram of (a-b) SL_2 - Cd_3As_2 , (c-d) SL_4 - Cd_3As_2 and (e-f) SL_6 - Cd_3As_2 as a function of δ/b and the SL periodicity a_{SL} . In panels (a-b), $a_x = a_{SL}$ and $a_y = 2a_{SL}$. The left (right) panels show the topological phase diagrams for positive (negative) values of the SL potential harmonics.

37, respectively. The topological phase diagrams are shown in Fig. 3. They mirror those in Fig. 2, with the sole distinction being the values at which the topological

phase transition takes place. Similar to the SL_n -BHZ case, we can see from Figs. 3(b) and 3(f) that a SL_2 and SL_6 with negative harmonics applied on $tfCd_3As_2$ lead to a topological phase even when the original phase is trivial. From Fig. 3(c), the SL_4 -tf Cd_3As_2 phase is topological for $0 < \delta < 2b\pi^2/a_{SL}^2$. The upper bound represents the line below which the rBZ encloses a Berry flux of 2π of the spin-up band. This agrees with Ref. [61], which studied a SL_4 with $a_{SL} = 50$ nm and, for V = 1meV, found the topological phase for a gap in the range 0 - 2meV, consistent with our bound evaluated at $a_{SL} = 50$ nm. An analogous conclusion holds for SL_6 -tf Cd_3As_2 .

Another example involves thin films of 3D topological insulator, such as ${\rm tfBi_2X_3}$ (X = Se, Te) or ${\rm tfSb_2Te_3}$ [74–77]. Their thickness is set by the number of quintuple layers N stacked vertically, i.e. $\eta=Na$ where a denotes the thickness of a single quintuple layer. Again, these systems can be modeled by Eq. 33, with each block having the form of Eq. 31 with $\xi_x=1$, $\xi_y=\xi$, $d_0=E_0-ck^2$, $d_x=vk_y$, $d_y=-vk_x$ and $d_z=\delta-bk^2$ [66, 67]. Without a SL potential, the gap of these materials is topological when ${\rm sgn}(\delta/b)=1$, yielding a quantum spin Hall state. Tab. III summarizes the

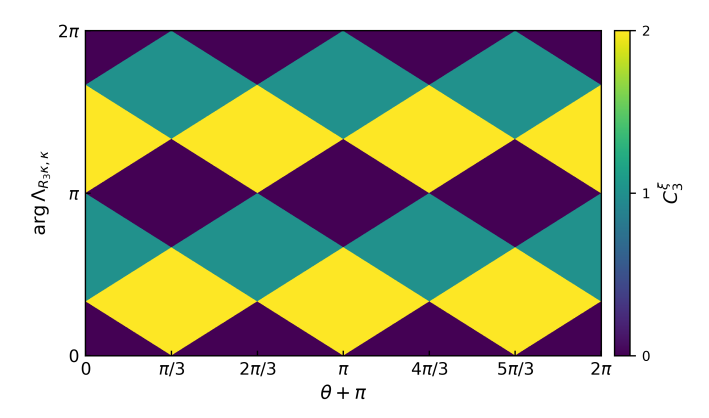


FIG. 4: Topological phase diagram of the valence miniband at the $\xi=-1$ valley of SL₃-TMD as a function of the argument of the form factor $\Lambda_{R_3\kappa,\kappa}$ and the phase of the superlattice potential θ .

parameter values at different thicknesses and the \mathbb{Z}_2 invariant when the system is subject to a SL potential. The sign of the harmonics of the applied SL can again be used to control the topological phase of the thin films. For example, $tfBi_2Se_3$ is trivial since $\delta/b < 0$ for all thicknesses. Therefore, applying a SL₂ and SL₆ potential with negative harmonics would induce a topological phase. Similarly, three- and four-layers of Bi₂Te₃ as well as two- and three-layers of Sb₂Te₃ can become topological when a $SL_{n=2,6}$ is applied. In contrast, twoand five-layers of Bi₂Te₃ and four-, five- and six- layers of Sb₂Te₃ are all topological in the absence of a SL, because $\delta/b > 0$, and a SL can be used to suppress this phase. Note that the formalism presented in this paper does not take into account inversion symmetry-breaking effects that can alter the magnitude and the sign of the gap, e.g., Rashba splitting. Hence, the topological phases predicted using our formalism are valid in the limit where these effects are negligible.

C. SL_n -TMD

We now turn to a superlattice imposed on TMDs. A key feature of these materials is the strong Ising spin splitting in the valence band of the K and K' valleys, implying that spin is essentially locked to valley in these bands. Since the two valleys are related by time-reversal symmetry, the low-energy physics in each valley separately breaks time-reversal. Thus, we seek the Chern number in each valley upon imposing the superlattice potential.

Expanding the band structure around the K or K' point yields a massive Dirac Hamiltonian

$$h_{\xi}(\mathbf{k}) = v(\sigma_x k_x + \xi \sigma_y k_y) + \Delta \sigma_z, \tag{41}$$

where v is the velocity and $\xi = \pm 1$ for K and K' valleys. This Hamiltonian takes the form of Eq. 31, with $\xi_x = 1$, $\xi_y = \xi$, $d_0 = 0$, $d_x = vk_x$, $d_y = v\xi k_y$ and $d_z = \Delta$. For TMDs, the parameter Δ , which is related to the gap, is always positive. Therefore, since we seek the topology of the valence band, we will consider the eigenfunctions of $-h_{\xi}$ which are given by Eq. 32 with $\mathbf{d} \to -\mathbf{d}$.

We then use the formalism of Sec. IV to compute the Chern number of the valence band of a single valley when the TMD is subject to a weak superlattice potential. The p-fold rotation operator has the same form as Eq. 38 with $J_z = \sigma_z/2$, which has two eigenvalues $\pm 1/2$. This representation allows for the direct computation of the form factors of the valence band: using Eqs. 5, 32 and 38, the form factors can be rewritten as

$$\Lambda_{R_p q, q}^{\xi} = \frac{\left\langle \Psi_{+}^{1, \xi}(-\mathbf{d}, q) \middle| U_p^{\dagger} \middle| \Psi_{+}^{1, \xi}(-\mathbf{d}, q) \right\rangle}{\left\langle \Psi_{+}^{1, \xi}(-\mathbf{d}, \gamma) \middle| U_p^{\dagger} \middle| \Psi_{+}^{1, \xi}(-\mathbf{d}, \gamma) \middle\rangle}$$

$$= \frac{e^{-2\pi i \xi/p} (d - d_z) + d + d_z}{2d}, \tag{42}$$

Since d_z is **k**-independent and d is a function of k^2 , the form factor depends only on q^2 , the distance between the high-symmetry point q and the γ point.

For n=2, which implies p=2, the form factor simplifies to $\Lambda_{R_2q,q}^\xi=\Delta/d$. Thus, the form factor is strictly real and positive, implying $\arg\Lambda_{R_2q,q}^\xi=0$. Moreover, because V_g is real for n=2, one can show that Eq. 30 gives

$$C_2^{\xi} = \Theta\left(V_{g_x} V_{g_y} V_{g_m}\right) \mod 2,\tag{43}$$

with $g_q=R_2q-q$ and where Θ represents the Heaviside step function. This demonstrates that the parity of the Chern number of the valence miniband at K and K' of SL_2 -TMD is independent of the superlattice periodicity and the material parameters v and Δ . The only requirement to obtain non-trivial topology is that the product of the harmonics at the three high-symmetry points is positive and the potential strength remains within the perturbative regime – crucially though, this requires that all harmonics be non-zero. Notice that since $C_2^{\xi=+1}=C_2^{\xi=-1}$, the total Chern number for both valleys $C_2=C_2^{\xi=+1}+C_2^{\xi=-1}\mod 2$ vanishes, as must be the case since $\mathcal T$ symmetry is preserved in the entire system.

For SL_3 -TMD, Eq. 30 gives the following Chern number

$$C_3^{\xi} = \sum_{q=\kappa,\kappa'} \left[\frac{\pi - 3\arg\left(-V_{g_q}\Lambda_{R_3q,q}^{\xi}\right)}{2\pi} \right] \mod 3. \tag{44}$$

In this situation, R_2 is not a symmetry element, so the harmonics are not real. Nevertheless, the C_3 symmetry requires that $V_{g_{\kappa'}} = V_{g_{\kappa}}^*$ with $V_{g_{\kappa}} = |V|e^{i\theta}$ and $g_{\kappa} = R_3\kappa - \kappa$. In addition, since the form factor depends only on the distance between its arguments, it follows that

	$v\hbar$ [eV·Å]	$\Delta \text{ [eV]}$	$\arg(\Lambda_{R_3\kappa,\kappa}^{\xi=-1})\cdot 10^3$	$\arg \Lambda_{R_4 m, m}^{\xi = -1} \cdot 10^3$
MoS_2	3.51	0.83	1.69	2.20
WS_2	4.38	0.90	2.24	2.90
$MoSe_2$	3.11	0.74	1.67	2.17
WSe_2	3.94	0.80	2.29	3.00
$MoTe_2$	3.26	0.55	3.32	4.30
WTe_2	3.10	0.50	3.63	4.70

TABLE IV: Numerical parameters of Eq. 41 for selected TMDs. The values of $v\hbar$ and Δ are taken from Ref. [63] for the TMDs involving the S and Se chalcogen and from Ref. [78] for those involving the Te chalcogen. The last two columns were obtained using a superlattice periodicity $a_{\rm SL}=20{\rm nm}$.

$$\Lambda_{R_3\kappa,\kappa}^{\xi} = \Lambda_{R_3\kappa',\kappa'}^{\xi}$$
. Therefore,

$$C_3^{\xi} = \sum_{n=\pm 1} \left[\frac{\pi - 3n(\theta + \pi) - 3\arg\Lambda_{R_3\kappa,\kappa}^{\xi}}{2\pi} \right] \mod 3.$$

Although Eq. 45 does not explicitly depend on the magnitude of |V|, our conclusions require that the highest energy valence band in the rBZ is gapped from other bands, which does depend on the magnitude of |V|.

Eq. 45 gives the topological phase diagram presented in Fig. 4. This figure shows that, in principle, various topological phases can be realized by varying the phase θ . However, when the experimentally relevant values of Δ , v and $a_{\rm SL}$ (the SL periodicity) are used, one finds that $\arg \Lambda_{R_3\kappa,\kappa}^{\xi=-1}$ is on the order of 10^{-3} (see Tab. IV), which implies that only a limited subset of the theoretically possible topological phases can be realized. More precisely, the only accessible non-trivial phase is $C_3^{\xi=-1}=2\mod 3$, which occurs only for $\theta=0,2\pi/3$ and $4\pi/3$. This is consistent with the discussion in [41, 58]. Furthermore, the occurrence of a topological phase at $\theta = 0$ and a trivial phase at $\theta = \pi$ is consistent with the findings of Ref. [59] for WSe₂ (note that $\theta = 0$ (π) is related to $V < 0 \ (V > 0)$ in Ref. [59]). The two additional topological phases at $\theta = 2\pi/3, 4\pi/3$ were not identified in Ref. [59] because only real superlattice harmonics were considered in that work.

For SL_4 -TMD, the two high-symmetry points of the rBZ under consideration are x and m. Since p(x)=2, it follows that the form factor $\Lambda_{R_2x,x}^{\xi}$ is real and positive, as in the SL_2 -TMD case. Then, the presence of the symmetry element R_2 ensures that the harmonics V_{g_x} and V_{g_m} are real, while the additional R_4 symmetry

requires that $V_{g_x} = V_{g_m}$. Consequently, Eq. 30 gives

$$C_4^{\xi} = 2\Theta(V_{g_m}) + \left[\frac{\pi - 4\arg\left(-V_{g_m}\Lambda_{R_4m,m}^{\xi}\right)}{2\pi} \right] \mod 4.$$

$$\tag{46}$$

When $V_{g_m} < 0$, the first term of the preceding equation vanishes, and a numerical evaluation yields $4 \arg \Lambda_{R_4 m,m}^{\xi} \sim 4 \cdot 10^{-3}$, indicating that $C_4^{\xi} = 0 \mod 4$ for all the TMDs of Tab. IV. Conversely, for $V_{g_m} > 0$, the loop phase is $4\pi + 4 \arg \Lambda_{R_4 m,m}^{\xi}$, so that $C_4^{\xi} = 0 \mod 4$. Thus, a square superlattice potential applied to a TMD cannot induce topology within the perturbative regime we consider.

Following the same line of reasoning for SL_6 -TMD, we arrive at the following expression for the Chern number

$$C_6^{\xi} = 3\Theta(V_{g_{\kappa}}) + 2\left[\frac{\pi - 3\arg\left(-V_{g_{\kappa}}\Lambda_{R_3\kappa,\kappa}^{\xi}\right)}{2\pi}\right] \mod 6.$$
(47)

For $V_{g_{\kappa}} < 0$, the phase is trivial for the TMDs considered. However, when $V_{g_{\kappa}} > 0$, we find $C_6^{\xi = -1} = 5 \mod 6$.

VI. CONCLUSION

introduced broadly applicable We a computationally efficient framework for predicting the topology of superlattice materials with spin-The approach combines degenerate orbit coupling. perturbation theory with the method of symmetry indicators, which extracts topological indices from symmetry eigenvalues. In practical terms, we provide a systematic prescription that takes as input only the leading harmonics of the superlattice potential together with a small set of material-specific coefficients. From these quantities, we derive analytic formulas for the \mathbb{Z}_2 invariant (in the presence of time-reversal and inversion symmetry) or Chern number (in the absence of time-reversal symmetry), allowing characterization of topological phases and without full superlattice bandstructure calculations. The method is readily scalable to a high-throughput search, transparent enough to expose the microscopic origin of nontrivial topology, and flexible across platforms.

One important outcome is that for two-fold and six-fold symmetric superlattices, topological superlattice bands can arise even when the parent material is not topological. This greatly expands the range of materials, or material parameters, e.g., film thickness, that can be explored to realize topological flat bands in engineered superlattices.

ACKNOWLEDGMENTS

The authors acknowledge a helpful conversation with Jiabin Yu. M.N.Y.L. acknowledges support from the National Science Foundation under the Columbia MRSEC on Precision-Assembled Quantum Materials (PAQM), Grant No. DMR-2011738. V.C. and J.C. acknowledge support from the Flatiron Institute, a division of the Simons Foundation. This work was performed in part at the Aspen Center for Physics, which is supported by National Science Foundation grant PHY-2210452.

Appendix A: Diagonalization of a block circulant matrix

Let b_j with j = 0, ..., n-1 be a set of $k \times k$ matrices. These matrices can be used to construct a block-circulant matrix $B \in \mathcal{BC}_{n,k}$ [79], such that

$$B = \text{circ}(b_0, b_1, \dots, b_{n-1}) = \sum_{j=0}^{n-1} S^j \otimes b_j,$$
 (A1)

- [1] R. Bistritzer and A. H. MacDonald, Moiré bands in twisted double-layer graphene, Proceedings of the National Academy of Sciences 108, 12233 (2011).
- [2] E. Y. Andrei, D. K. Efetov, P. Jarillo-Herrero, A. H. MacDonald, K. F. Mak, T. Senthil, E. Tutuc, A. Yazdani, and A. F. Young, The marvels of moiré materials, Nature Reviews Materials 6, 201 (2021).
- [3] K. P. Nuckolls and A. Yazdani, A microscopic perspective on moiré materials, Nature Reviews Materials 9, 460 (2024).
- [4] C. Forsythe, X. Zhou, K. Watanabe, T. Taniguchi, A. Pasupathy, P. Moon, M. Koshino, P. Kim, and C. R. Dean, Band structure engineering of 2d materials using patterned dielectric superlattices, Nature nanotechnology 13, 566 (2018).
- [5] B. S. Jessen, L. Gammelgaard, M. R. Thomsen, D. M. Mackenzie, J. D. Thomsen, J. M. Caridad, E. Duegaard, K. Watanabe, T. Taniguchi, T. J. Booth, et al., Lithographic band structure engineering of graphene, Nature nanotechnology 14, 340 (2019).
- [6] Y. Li, S. Dietrich, C. Forsythe, T. Taniguchi,

where we used the cyclic right-shift matrix

$$S = \begin{pmatrix} 0 & 0 & \dots & 0 & 1 \\ 1 & 0 & \dots & 0 & 0 \\ 0 & 1 & \dots & 0 & 0 \\ \vdots & \vdots & \ddots & \vdots & \vdots \\ 0 & 0 & \dots & 1 & 0 \end{pmatrix}, \tag{A2}$$

which satisfies $S^n = \mathbb{I}_n$. The vector $v_j = (x, \omega^j x, \omega^{2j} x, \dots, \omega^{(n-1)j} x)^T$, with $\omega = e^{2\pi i/n}$ the *n*-th root of unity and $x \in \mathbb{C}^k$, satisfies

$$S^l \otimes \mathbb{I}_k v_j = \omega^{-lj} v_j. \tag{A3}$$

Thus, v_i satisfies

$$Bv_i = \mathbb{I}_n \otimes \lambda_i v_i, \tag{A4}$$

where $\lambda_j = \sum_{m=0}^{n-1} b_m \omega^{-mj}$ is a $k \times k$ matrix. The spectrum of B is then obtained by diagonalising the matrices λ_j ; if y is an eigenvector of λ_j with eigenvalue μ , then μ is an eigenvalue of B with eigenvector v_j constructed from x = y.

The projected Hamiltonian, Eq. 9 in the main text, is precisely a block-circulant matrix, i.e. $PHP \in \mathcal{BC}_{p,2}$. Its diagonalization is straightforward, since one can always choose a basis in which PHP is expressed in a block diagonal basis, which implies that there is only one block to diagonalize. The calculation shown in this appendix is intended for the complementary case, when no such basis exists, i.e. when the matrix cannot be reduced to a block-diagonal form. The spectrum of a matrix $B \in \mathcal{BC}_{n,1}$ that is circulant, i.e. when $b_j \in \mathbb{C}$, is obtained in a similar manner: the eigenvectors are the vectors v_j with x = 1 and λ_j are the associated eigenvalues.

- K. Watanabe, P. Moon, and C. R. Dean, Anisotropic band flattening in graphene with one-dimensional superlattices, Nature Nanotechnology 16, 525 (2021).
- [7] D. Barcons Ruiz, H. Herzig Sheinfux, R. Hoffmann, I. Torre, H. Agarwal, R. K. Kumar, L. Vistoli, T. Taniguchi, K. Watanabe, A. Bachtold, et al., Engineering high quality graphene superlattices via ion milled ultra-thin etching masks, Nature communications 13, 6926 (2022).
- [8] J. Sun, S. A. Akbar Ghorashi, K. Watanabe, T. Taniguchi, F. Camino, J. Cano, and X. Du, Signature of correlated insulator in electric field controlled superlattice, Nano Letters 24, 13600 (2024).
- [9] M. Killi, S. Wu, and A. Paramekanti, Band structures of bilayer graphene superlattices, Phys. Rev. Lett. 107, 086801 (2011).
- [10] J. C. Song, P. Samutpraphoot, and L. S. Levitov, Topological bloch bands in graphene superlattices, Proceedings of the National Academy of Sciences 112, 10879 (2015).
- [11] E. M. Spanton, A. A. Zibrov, H. Zhou, T. Taniguchi,

- K. Watanabe, M. P. Zaletel, and A. F. Young, Observation of fractional chern insulators in a van der waals heterostructure, Science **360**, 62 (2018).
- [12] F. Wu, T. Lovorn, E. Tutuc, and A. H. MacDonald, Hubbard model physics in transition metal dichalcogenide moiré bands, Phys. Rev. Lett. 121, 026402 (2018).
- [13] A. L. Sharpe, E. J. Fox, A. W. Barnard, J. Finney, K. Watanabe, T. Taniguchi, M. Kastner, and D. Goldhaber-Gordon, Emergent ferromagnetism near three-quarters filling in twisted bilayer graphene, Science 365, 605 (2019).
- [14] G. Tarnopolsky, A. J. Kruchkov, and A. Vishwanath, Origin of magic angles in twisted bilayer graphene, Phys. Rev. Lett. 122, 106405 (2019).
- [15] F. Wu, T. Lovorn, E. Tutuc, I. Martin, and A. H. MacDonald, Topological insulators in twisted transition metal dichalcogenide homobilayers, Phys. Rev. Lett. 122, 086402 (2019).
- [16] B. L. Chittari, G. Chen, Y. Zhang, F. Wang, and J. Jung, Gate-tunable topological flat bands in trilayer graphene boron-nitride moiré superlattices, Phys. Rev. Lett. 122, 016401 (2019).
- [17] Y.-H. Zhang, D. Mao, Y. Cao, P. Jarillo-Herrero, and T. Senthil, Nearly flat chern bands in moiré superlattices, Phys. Rev. B 99, 075127 (2019).
- [18] M. Serlin, C. Tschirhart, H. Polshyn, Y. Zhang, J. Zhu, K. Watanabe, T. Taniguchi, L. Balents, and A. Young, Intrinsic quantized anomalous Hall effect in a moiré heterostructure, Science 367, 900 (2020).
- [19] K. P. Nuckolls, M. Oh, D. Wong, B. Lian, K. Watanabe, T. Taniguchi, B. A. Bernevig, and A. Yazdani, Strongly correlated chern insulators in magic-angle twisted bilayer graphene, Nature 588, 610 (2020).
- [20] D. Muñoz-Segovia, V. Crépel, R. Queiroz, and A. J. Millis, Twist-angle evolution of the intervalley-coherent antiferromagnet in twisted wse 2, Phys. Rev. B 112, 085111 (2025).
- [21] H. Pan, F. Wu, and S. Das Sarma, Band topology, Hubbard model, Heisenberg model, and Dzyaloshinskii-Moriya interaction in twisted bilayer wse₂, Phys. Rev. Res. 2, 033087 (2020).
- [22] Y. Xie, A. T. Pierce, J. M. Park, D. E. Parker, E. Khalaf, P. Ledwith, Y. Cao, S. H. Lee, S. Chen, P. R. Forrester, K. Watanabe, T. Taniguchi, A. Vishwanath, P. Jarillo-Herrero, and A. Yacoby, Fractional chern insulators in magic-angle twisted bilayer graphene, Nature 600, 439 (2021).
- [23] V. Crépel and N. Regnault, Attractive haldane bilayers for trapping non-abelian anyons, Phys. Rev. B 110, 115109 (2024).
- [24] J. Cano, S. Fang, J. H. Pixley, and J. H. Wilson, Moiré superlattice on the surface of a topological insulator, Phys. Rev. B 103, 155157 (2021).
- [25] T. Wang, N. F. Q. Yuan, and L. Fu, Moiré surface states and enhanced superconductivity in topological insulators, Phys. Rev. X 11, 021024 (2021).
- [26] T. Devakul, V. Crépel, Y. Zhang, and L. Fu, Magic in twisted transition metal dichalcogenide bilayers, Nature communications 12, 6730 (2021).
- [27] Y. Zhang, T. Devakul, and L. Fu, Spin-textured Chern bands in AB-stacked transition metal dichalcogenide bilayers, Proceedings of the National Academy of Sciences 118, e2112673118 (2021).

- [28] D. Guerci, J. Wang, J. H. Pixley, and J. Cano, Designer meron lattice on the surface of a topological insulator, Phys. Rev. B 106, 245417 (2022).
- [29] H. Pan, M. Xie, F. Wu, and S. Das Sarma, Topological phases in AB-stacked MoTe₂/WSe₂: z₂ topological insulators, Chern insulators, and topological charge density waves, Phys. Rev. Lett. 129, 056804 (2022).
- [30] Z.-D. Song and B. A. Bernevig, Magic-angle twisted bilayer graphene as a topological heavy fermion problem, Phys. Rev. Lett. 129, 047601 (2022).
- [31] H. Park, J. Cai, E. Anderson, Y. Zhang, J. Zhu, X. Liu, C. Wang, W. Holtzmann, C. Hu, Z. Liu, T. Taniguchi, K. Watanabe, J.-H. Chu, T. Cao, L. Fu, W. Yao, C.-Z. Chang, D. Cobden, D. Xiao, and X. Xu, Observation of fractionally quantized anomalous Hall effect, Nature 622, 74 (2023).
- [32] Y. Zeng, Z. Xia, K. Kang, J. Zhu, P. Knüppel, C. Vaswani, K. Watanabe, T. Taniguchi, K. F. Mak, and J. Shan, Thermodynamic evidence of fractional chern insulator in moirémote2, Nature 622, 69 (2023).
- [33] F. Xu, Z. Sun, T. Jia, C. Liu, C. Xu, C. Li, Y. Gu, K. Watanabe, T. Taniguchi, B. Tong, J. Jia, Z. Shi, S. Jiang, Y. Zhang, X. Liu, and T. Li, Observation of integer and fractional quantum anomalous hall effects in twisted bilayer mote₂, Phys. Rev. X 13, 031037 (2023).
- [34] S. A. A. Ghorashi, A. Dunbrack, A. Abouelkomsan, J. Sun, X. Du, and J. Cano, Topological and stacked flat bands in bilayer graphene with a superlattice potential, Phys. Rev. Lett. 130, 196201 (2023).
- [35] V. Crépel and A. Millis, Spinon pairing induced by chiral in-plane exchange and the stabilization of odd-spin chern number spin liquid in twisted mote 2, Phys. Rev. Lett. 133, 146503 (2024).
- [36] S. A. A. Ghorashi and J. Cano, Multilayer graphene with a superlattice potential, Phys. Rev. B 107, 195423 (2023).
- [37] N. Morales-Durán, J. Wang, G. R. Schleder, M. Angeli, Z. Zhu, E. Kaxiras, C. Repellin, and J. Cano, Pressureenhanced fractional chern insulators along a magic line in moiré transition metal dichalcogenides, Phys. Rev. Res. 5, L032022 (2023).
- [38] A. De Martino, L. Dell'Anna, L. Handt, A. Miserocchi, and R. Egger, Two-dimensional dirac fermions in a mass superlattice, Phys. Rev. B 107, 115420 (2023).
- [39] V. Crépel, A. Dunbrack, D. Guerci, J. Bonini, and J. Cano, Chiral model of twisted bilayer graphene realized in a monolayer, Phys. Rev. B 108, 075126 (2023).
- [40] Z. Lu, T. Han, Y. Yao, A. P. Reddy, J. Yang, J. Seo, K. Watanabe, T. Taniguchi, L. Fu, and L. Ju, Fractional quantum anomalous hall effect in multilayer graphene, Nature 626, 759 (2024).
- [41] Y. Zeng, T. M. R. Wolf, C. Huang, N. Wei, S. A. A. Ghorashi, A. H. MacDonald, and J. Cano, Gate-tunable topological phases in superlattice modulated bilayer graphene, Phys. Rev. B 109, 195406 (2024).
- [42] D. Seleznev, J. Cano, and D. Vanderbilt, Inducing topological flat bands in bilayer graphene with electric and magnetic superlattices, Phys. Rev. B 110, 205115 (2024).
- [43] K. Yang, Z. Xu, Y. Feng, F. Schindler, Y. Xu, Z. Bi, B. A. Bernevig, P. Tang, and C.-X. Liu, Topological minibands and interaction driven quantum anomalous hall state in topological insulator based moiré heterostructures, Nature communications 15, 2670 (2024).

- [44] J. Shi, J. Cano, and N. Morales-Durán, Effects of berry curvature on ideal band magnetorotons, arXiv preprint arXiv:2503.15900 (2025).
- [45] J. Xie, Z. Huo, X. Lu, Z. Feng, Z. Zhang, W. Wang, Q. Yang, K. Watanabe, T. Taniguchi, K. Liu, Z. Song, X. C. Xie, J. Liu, and X. Lu, Tunable fractional chern insulators in rhombohedral graphene superlattices, Nature Materials 10.1038/s41563-025-02225-7 (2025).
- [46] Y. H. Kwan, J. Yu, J. Herzog-Arbeitman, D. K. Efetov, N. Regnault, and B. A. Bernevig, Moiré fractional chern insulators. iii. hartree-fock phase diagram, magic angle regime for chern insulator states, role of moiré potential, and goldstone gaps in rhombohedral graphene superlattices, Physical Review B 112, 075109 (2025).
- [47] K. Uchida, S. Furuya, J.-I. Iwata, and A. Oshiyama, Atomic corrugation and electron localization due to moiré patterns in twisted bilayer graphenes, Phys. Rev. B 90, 155451 (2014).
- [48] J. Jung, A. Raoux, Z. Qiao, and A. H. MacDonald, Ab initio theory of moiré superlattice bands in layered twodimensional materials, Phys. Rev. B 89, 205414 (2014).
- [49] S. Carr, D. Massatt, S. Fang, P. Cazeaux, M. Luskin, and E. Kaxiras, Twistronics: Manipulating the electronic properties of two-dimensional layered structures through their twist angle, Phys. Rev. B 95, 075420 (2017).
- [50] Y. Zhang, T. Liu, and L. Fu, Electronic structures, charge transfer, and charge order in twisted transition metal dichalcogenide bilayers, Phys. Rev. B 103, 155142 (2021).
- [51] T. Zhang, N. Regnault, B. A. Bernevig, X. Dai, and H. Weng, o(n) ab initio calculation scheme for large-scale moiré structures, Phys. Rev. B **105**, 125127 (2022).
- [52] L. Fu and C. L. Kane, Topological insulators with inversion symmetry, Phys. Rev. B 76, 045302 (2007).
- [53] C. Fang, M. J. Gilbert, and B. A. Bernevig, Bulk topological invariants in noninteracting point group symmetric insulators, Phys. Rev. B 86, 115112 (2012).
- [54] B. Bradlyn, L. Elcoro, J. Cano, M. G. Vergniory, Z. Wang, C. Felser, M. I. Aroyo, and B. A. Bernevig, Topological quantum chemistry, Nature 547, 298 (2017).
- [55] H. C. Po, A. Vishwanath, and H. Watanabe, Symmetrybased indicators of band topology in the 230 space groups, Nature communications 8, 50 (2017).
- [56] J. Cano, B. Bradlyn, Z. Wang, L. Elcoro, M. G. Vergniory, C. Felser, M. I. Aroyo, and B. A. Bernevig, Building blocks of topological quantum chemistry: Elementary band representations, Phys. Rev. B 97, 035139 (2018).
- [57] J. Cano and B. Bradlyn, Band representations and topological quantum chemistry, Annual Review of Condensed Matter Physics 12, 225 (2021).
- [58] V. Crépel and J. Cano, Efficient prediction of superlattice and anomalous miniband topology from quantum geometry, Phys. Rev. X 15, 011004 (2025).
- [59] L.-k. Shi, J. Ma, and J. C. W. Song, Gate-tunable flat bands in van der waals patterned dielectric superlattices, 2D Materials 7, 015028 (2019).
- [60] K. Yang, Z. Xu, Y. Feng, F. Schindler, Y. Xu, Z. Bi, B. A. Bernevig, P. Tang, and C.-X. Liu, Topological minibands and interaction driven quantum anomalous hall state in topological insulator based moiré heterostructures, Nature communications 15, 2670 (2024).
- [61] W. Miao, A. Rashidi, and X. Dai, Artificial moiré engineering for an ideal BHZ model, arXiv preprint

- arXiv:2409.08540 (2024).
- [62] K. Yang, Y. Liu, F. Schindler, and C.-X. Liu, Engineering miniband topology via band folding in moiré superlattice materials, Phys. Rev. B 111, L241104 (2025).
- [63] D. Xiao, G.-B. Liu, W. Feng, X. Xu, and W. Yao, Coupled spin and valley physics in monolayers of mos₂ and other group-vi dichalcogenides, Phys. Rev. Lett. 108, 196802 (2012).
- [64] B. A. Bernevig, T. L. Hughes, and S.-C. Zhang, Quantum spin hall effect and topological phase transition in hgte quantum wells, Science 314, 1757 (2006).
- [65] W. Miao, B. Guo, S. Stemmer, and X. Dai, Engineering the in-plane anomalous hall effect in cd₃as₂ thin films, Phys. Rev. B 109, 155408 (2024).
- [66] W.-Y. Shan, H.-Z. Lu, and S.-Q. Shen, Effective continuous model for surface states and thin films of three-dimensional topological insulators, New Journal of Physics 12, 043048 (2010).
- [67] S.-Q. Shen, Topological insulators, Vol. 174 (Springer, 2012).
- [68] Y. Liu, K. Yang, C.-X. Liu, and J. Yu, Symmetry-enforced moiré topology, arXiv preprint arXiv:2509.06906 (2025).
- [69] C. L. Kane and E. J. Mele, Z₂ topological order and the quantum spin hall effect, Phys. Rev. Lett. 95, 146802 (2005).
- [70] C.-X. Liu, H. Zhang, B. Yan, X.-L. Qi, T. Frauenheim, X. Dai, Z. Fang, and S.-C. Zhang, Oscillatory crossover from two-dimensional to three-dimensional topological insulators, Phys. Rev. B 81, 041307 (2010).
- [71] Z. Wang, H. Weng, Q. Wu, X. Dai, and Z. Fang, Threedimensional Dirac semimetal and quantum transport in Cd₃As₂, Phys. Rev. B 88, 125427 (2013).
- [72] E. Zsurka, C. Wang, J. Legendre, D. Di Miceli, L. m. c. Serra, D. Grützmacher, T. L. Schmidt, P. Rüßmann, and K. Moors, Low-energy modeling of three-dimensional topological insulator nanostructures, Phys. Rev. Mater. 8, 084204 (2024).
- [73] A. C. Lygo, B. Guo, A. Rashidi, V. Huang, P. Cuadros-Romero, and S. Stemmer, Two-dimensional topological insulator state in cadmium arsenide thin films, Phys. Rev. Lett. 130, 046201 (2023).
- [74] Y. Zhang, K. He, C.-Z. Chang, C.-L. Song, L.-L. Wang, X. Chen, J.-F. Jia, Z. Fang, X. Dai, W.-Y. Shan, et al., Crossover of the three-dimensional topological insulator bi2se3 to the two-dimensional limit, Nature Physics 6, 584 (2010).
- [75] Y. Sakamoto, T. Hirahara, H. Miyazaki, S.-i. Kimura, and S. Hasegawa, Spectroscopic evidence of a topological quantum phase transition in ultrathin bi₂se₃ films, Phys. Rev. B 81, 165432 (2010).
- [76] Y.-Y. Li, G. Wang, X.-G. Zhu, M.-H. Liu, C. Ye, X. Chen, Y.-Y. Wang, K. He, L.-L. Wang, X.-C. Ma, et al., Intrinsic topological insulator bi2te3 thin films on si and their thickness limit, Advanced materials 22, 4002 (2010).
- [77] G. Wang, X. Zhu, J. Wen, X. Chen, K. He, L. Wang, X. Ma, Y. Liu, X. Dai, Z. Fang, et al., Atomically smooth ultrathin films of topological insulator sb2te3, Nano Research 3, 874 (2010).
- [78] A. Kormányos, G. Burkard, M. Gmitra, J. Fabian, V. Zólyomi, N. D. Drummond, and V. Fal'ko, k · p theory for two-dimensional transition metal dichalcogenide semiconductors, 2D Materials 2, 022001 (2015).

 $[79]\,$ G. J. Tee, Eigenvectors of block circulant and alternating

circulant matrices, New Zealand Journal of Mathematics ${\bf 36},\,195$ (2007).